Optimized Stokes imaging for highly resolved optical speckle fields, Part I: optimized experimental setup

Jonathan Staes, Julien Fade

To cite this version:

Jonathan Staes, Julien Fade. Optimized Stokes imaging for highly resolved optical speckle fields, Part I: optimized experimental setup. Journal of the Optical Society of America. A Optics, Image Science, and Vision, 2024, 41 (5), pp.789. 10.1364/josaa.516693 . hal-04596342

HAL Id: hal-04596342
https://hal.science/hal-04596342v1

Submitted on 14 Nov 2024

Optimized Stokes imaging for highly resolved optical speckle fields, part I: Optimized experimental setup

Jonathan Staes,[1] **and Julien Fade**[1,2,*]

[1] *Univ Rennes, CNRS, Institut FOTON - UMR 6082, F-35000 Rennes, France*
[2] *Aix-Marseille Univ, CNRS, Centrale Med, Institut Fresnel, Marseille, France*
[*] *julien.fade@fresnel.fr*

Abstract: In this first article of a three-paper series focusing on Stokes polarimetry of optical speckle fields resolved at the individual speckle grain scale, a review of the state of the art techniques for such experimental investigations is first provided. An optimized experimental setup is then extensively described which allows polarimetric Stokes measurements on such complex interference patterns to be carried out at each location of the speckle field without disturbing the wavefront. Specific calibration procedures are also described in order to provide the estimation of trustful polarimetric properties of light across a resolved speckle field.

1. Introduction

The phenomenon of speckle, very well-known in coherent optics, can be observed at the surface of a material when a coherent light source, such as laser light, illuminates a rough surface or propagates through a complex and/or random medium. The speckle pattern, an example of which is shown in Fig. 1, is made of more or less bright zones, termed speckle *grains*, which result from the constructive and destructive interferences of light components being scattered by the random medium. More precisely, a "grain" corresponds to an area of spatial coherence across the optical light field observed. Such phenomenon attracted an intense research in statistical optics to model and predict the characteristics of such complex interference patterns (size, shape, dynamic, polarization/coherence properties,...), resorting to stochastic (random) modeling of the light-matter interaction. Although commonly seen as a source of noise limiting the image quality [1–4] in the context of coherent imaging, the sensitivity of the speckle pattern, as an interferometric phenomenon, has enabled uncountable applications of speckle-based metrology or imaging modalities, especially in the biomedical domain with laser speckle contrast imaging for instance [5, 6].

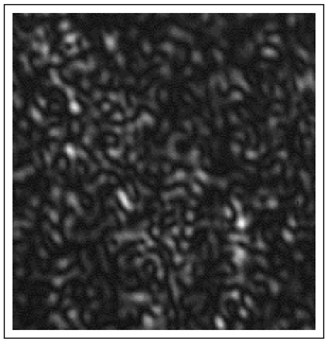

Fig. 1. Example of speckle pattern obtained by illuminating a scattering material (Spectralon) with a laser and imaging the backscattered field on a camera.

Besides theoretical characterization and practical applications of the speckle phenomenon, the polarization properties of speckle patterns has also been a domain of interest for research, either theoretically [7–9], or for more applied purposes [10–12]. In particular, in the context of active coherent polarimetric imaging, the phenomenon of depolarization of a polarized light field by a rough surface has led to a fertile scientific literature [13–15]. Indeed, the depolarization process not only depends on the optical and structural properties of the imaged object, but also depends on the experimental conditions (illumination, detection...) in which it is observed. If the depolarization properties were well known and understood at a macroscopic scale, i.e., when the speckle grains are properly "averaged" over the surface of the detector or the pixel, the situation was observed to be different when the size of the speckle grains become equal or greater than a pixel of the detector, i.e., when the speckle pattern is "resolved" by the camera. Due to the high sensitivity to all experimental conditions of speckle interference patterns, such observations were issued from statistical analyses of experimental data, without a clear understanding of the deterministic spatial distribution of the polarization state across the speckle field. This motivated the development of specific imaging setups and measurement protocols able to perform full-Stokes imaging analysis of the polarization properties of a highly resolved speckle pattern, at a highly "sub-speckle grain" scale, i.e., with speckle grains covering hundreds or thousands of pixels [16–18]. This article series focuses on this specific domain, and provides an optimal instrumental and processing design to perform such measurements with best accuracy, precision and robustness.

This paper is the first of a series of three joint articles, describing an optimized experimental study of the polarimetric properties of highly resolved multiscale speckle patterns, including the description of the optimized experimental setup used, a theoretical/simulation study to devise optimized sensing/data processing in this particular context, and lastly, original results including the proposal of new vizualisation modalities to represent polarimetric information (and especially polarimetric information in the vicinity of field polarization singularities). More precisely, this series of articles can be decomposed as follows:

Part 1: Experimental setup: In the present article, we first provide in Section 2 a short review of the previous works in polarization metrology of highly resolved speckle fields in the optical domain. We then technically detail in Section 3 the experimental setup used to perform the full-Stokes polarimetric analysis of the speckle pattern in a highly resolved manner. We then detail the automated acquisition procedure involving the so-called "SOPAFP" approach that will be detailed below, along with the processing strategy for the generation of a so-called photometric image. Such processing includes a dedicated calibration protocol used to correct the defects of the camera, while enabling high-dynamic range imaging on the intensity images acquired experimentally. Finally, we present in Section 6 preliminary results confirming the validity of the setup and of the calibration/processing/measurement approach used.

Part 2: Optimal acquisition & estimation strategies: The second paper of this series [19] presents a theoretical and numerical simulation study of the optimal sensing and processing strategies for highly resolved polarimetric analysis of a speckle pattern in the optical domain. These results allow us to clearly justify, for the first time to our best knowledge, the clear interest of the SOPAFP approach with respect to more classical sensing modalities, in particular to ensure best robustness of the estimated polarimetric states with respect to experimental imperfections (alignment, calibration defect, temperature drift...). This second paper provides a clear justification of the technical choices involved in the experimental setup that are be described below in the first article of this series.

Part 3: Topological analysis of polarimetric states distribution with optimized data representations: In the last article of the series [20], original experimental results issued from the optimized experimental bench developed are presented, allowing us to confirm previous conclusions from anterior works, and to exhibit interesting structures of polarization state distributions in the vicinity of field polarization singularities in the speckle pattern. This third article also provides a discussion abount the different available choices for multi-scale graphical representations of the polarimetric information, and a preferred original representation based on a specific planisheric projection is proposed and used.

2. State of the art of highly resolved Stokes imaging at the speckle grain scale

As stated above, questioning the depolarization phenomenon in the context of coherent light and speckled images justified the development of specific imaging instruments to measure the distribution of polarization states across a highly resolved speckle pattern. To our best knowledge, the first highly resolved Stokes imaging system at the speckle grain scale in the optics domain was developed in 2011 and reported by Pouget *et al.* [16]. This first contribution made it possible to highlight the many experimental difficulties of studying such a the speckle pattern locally because of its utmost sensitivity to all experimental conditions (air flow, temperature drift, vibration, laser stability, movement of optical components...), and proposed original ways to circumvent these difficulties. Highly resolved speckle patterns ($\sim 10^3$ pixels per grain) were obtained by imaging the sample under study through a 200 μm pinhole. To estimate the complete polarimetric state at each location of the speckle pattern, Stokes imaging was performed, which consists in measuring the 4-component Stokes vector (which completely describes the polarization state [21]) through various intensity image acquisitions performed with different configuration of a polarization-analyzing component. In this work, a polarization state analyzer (PSA) consisting of a retarding (quarter-wave) plate and a linear polarizer were placed in front of the detector. To probe several polarimetric states, mechanically rotation of the PSA was necessary, which implied tiny modifications of the optical path, which showed sufficient to modify the wavefront at the surface of the detector, and hence modify the speckle pattern that was under study. Despite the experimental difficulties and using a specific wavefront "recovery" protocol [16], this first dedicated experimental setup made it possible to experimentally compare the degree of polarization (DOP) at multiple scales and thus experimentally analyze the evolution of the DOP from an unresolved speckle pattern to a resolved one [16]. More importantly, this work established the first experimental confirmation (to our knowledge in the optics domain) of the fact that, for a perfectly static sample under continuous single-mode laser illumination, the polarization state at the grain scale is perfectly deterministic, i.e., with a degree of polarization (DOP) equal to 1. It also confirmed the previous statistical studies which stated that depolarization in this context of coherent imaging resulted from a spatial averaging (*spatial depolarization*) at the surface of the detector (pixel) of speckle grains having each a specific and deterministic polarization state. This work also allowed to study experimentally for the first time polarimetric states “trajectories” at the transition between two contiguous grains.

In 2013, a similar experimental bench was developed by Ghabbach *et al.*, but this setup included a voltage-controlled liquid crystal cell, which behaved as a polarimetric rotator [17]. Such configuration eliminates the need for any moving parts in the PSA, thereby ensuring the best preservation of the optical path during polarimetric analysis. This setup, with a resolution of the order of a few hundreds pixels per grain, demonstrated the interest of using liquid crystal variable retarders (LCVR) to optimize the preservation of the wavefront, and confirmed the abovementioned experimental observations. With this setup, a study of the polarization properties of a speckle pattern using an unpolarized coherent illumination made it possible to experimentally observe the so-called "repolarization" phenomenon obtained when a diffusing sample (assumed to be totally depolarizing) is illuminated by a totally unpolarized coherent source [22, 23]. In this situation, the expected and measured value of the spatial average of the DOP is 3/4. Although this phenomenon may be surprising given the depolarizing nature of the sample, it can be explained theoretically by modelling the depolarized beam as the sum of two linearly polarized waves, orthogonal to each other, and incoherent with each other.

Another setup was developed in 2014 by Dupont *et al.* [18,24] relying also on voltage controlled LCVRs to avoid any moving part. In this work, an original sensing approach was used to estimate the Stokes vector at each pixel by probing numerous polarimetric states distributed over the surface of the Poincaré's sphere that maps all possible perfectly polarized states of light across a unit sphere. This method was termed SOPAFP (for State Of Polarization Analysis by Full Projection), and will be described in detail below in this paper and in the second article of this series [19], as we shall use this approach for Stokes imaging. According to the first experimental results, this approach makes it possible to carry out a more accurate polarimetric analysis of the speckle pattern experimentally [18]. This work has also enabled polarimetric singularities to be studied experimentally [24].

In this article series, we present an updated version of the seminal setup developed at University of Rennes [16], including the advances proposed by the abovementioned contributors to this field. We also establish through numerical simulations how the SOPAFP can be optimized in its implementation in order to guarantee best estimation precision, accuracy and robustness [19]. We also present new experimental results and new representation modalities of the polarimetric information that are best adapted to this particular domain of investigation [20].

3. Optimized experimental setup

3.1. General overview of the experimental setup

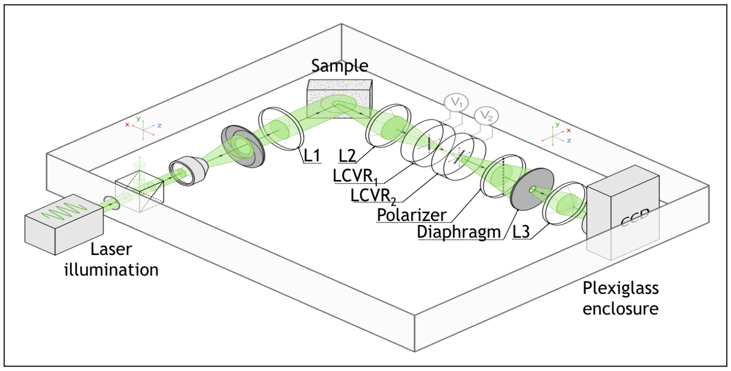

Fig. 2. Representation of the polarimetric imaging bench resolved at the speckle grain scale. For the sake of readability, the alignment mirrors between the laser source and the thermalization enclosure are not shown. In addition, the angle between the beam incident on the sample and the polarimetric analyzer is exaggerated here (90° in the figure, whereas 15° was implemented in the actual experiment to remain in a quasi monostatic configuration).

In order to gain better understanding of the depolarization/repolarization processes within the grains of a speckle pattern or to study polarization state distributions/transitions between grains or at the vicinity of field singularities, some hardware improvements to the initial polarimetric imaging bench described in [16] have been made and are detailed in this section. The existing setup has been installed in a plexiglass enclosure, itself placed on an air-cushioned optical table to minimize, respectively, the variations of the airflow in the optical path, and mechanical vibrations that can modify the interference pattern, as shown in [16]. In addition, this makes it possible to temperature-stabilize the whole experiment, thereby ensuring further long-term mechanical stability, but also stability of the optical response of the LCVR which is significantly temperature-dependent. The temperature of the enclosure was regulated at 26°C, a few degrees above the ambient temperature, using an on/off control and a heating cord, providing a ±1° stability over long periods of time. Yet, before each experimental acquisition, a thermalization step lasting around twenty minutes was carried out, in order to compensate for the additional heating of the setup by the laser illumination on the sample.

The various elements and characteristics of the imaging setup are now detailed in the following subsections.

3.2. Laser illumination and samples

The illumination source is a highly coherent frequency-doubled optically pumped Nd:YVO_4 laser (COHERENT Verdi V12) with a coherence length of ~100 m and a wavelength of 532 nm. A calcite Glan polarizer is placed at the entrance of the setup to ensure perfect vertical linear polarization of the beam (typical extinction ration 1:100,000), which undergoes several mirror reflections to convey the beam from the laser to the setup entrance (these mirrors are not shown in Fig.2). A telescopic arrangement of a microscope objective (x10, 0.25 NA, OLYMPUS), a diaphragm and a convex lens L1 (f=200 mm) makes it possible to control the width of the homogneneous collimated beam used to shine the sample, and to eliminate unwanted reflections/diffraction artifacts. The aperture of the diaphragm is adjusted so as to obtain a uniform spot of light on the sample of 2.5 cm in diameter.

The samples that have been studied consist of thick metallic plates, marble blocks of different colours obtained with an homogenous layer of spray paint and a Spectralon reflectance standard. These samples allowed us to perform experiments on opaque reflective/scattering materials with various depolarization properties ranging from non depolarizing to totally depolarizing samples. For each sample, preliminary thermalization was carried out as mentioned above.

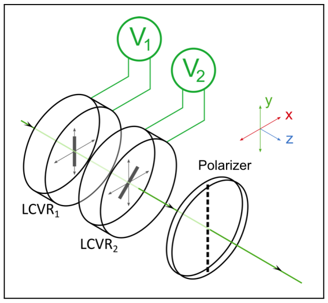

Fig. 3. Representation of the polarimetric analyzer based on voltage-controlled liquid crystal variable retarder (LCVR) plates.

3.3. Polarization analysis and imaging devices

On the light analysis/detection side, the imager consists of a polarimetric state analyser (PSA) placed between two converging lenses (L2 (f=80 mm) and L3 (f=40 mm)), the whole PSA being located upstream of the image sensor. In order to ensure similar conditions as coherent imaging applications, the sample plane is conjugated with an intermediate image plane located at the center of the PSA using the first converging lens L2. This intermediate image plane is finally itself conjugated with the sensor plane with lens L3. As a result, the sample and the sensor are located in conjugate planes, ensuring an imaging configuration of speckle observation, also termed *subjective speckle* [25].

3.3.1. Polarization State Analyzer (PSA)

The PSA consists of two voltage-controlled, temperature-stabilized LCVR (MAEDOWLARK), named $LCVR_1$ and $LCVR_2$, and of a linear polarizer (Thorlabs). These two LCVRs have been adjusted so that their fast axes are aligned respectively along the vertical axis (parallel to the illumination polarization direction) and at −45° from the horizontal axis in a clockwise direction, as shown in Fig. 3. As for the polarizer, its axis is aligned vertically. Thus the Mueller matrix of such PSA is theoretically given by:

$$M_{PSA} = \frac{1}{2}\begin{pmatrix} 1 & -cos(\phi_2) & sin(\phi_1)sin(\phi_2) & -cos(\phi_1)sin(\phi_2) \\ -1 & cos(\phi_2) & -sin(\phi_1)sin(\phi_2) & cos(\phi_1)sin(\phi_2) \\ 0 & 0 & 0 & 0 \\ 0 & 0 & 0 & 0 \end{pmatrix} \tag{1}$$

where ϕ_1 and ϕ_2 represent the phase shifts introduced respectively on $LCVR_1$ and $LCVR_2$ when a voltage pair V_{LCVR1} and V_{LCVR2} is applied. After a meticulous alignment step, the LCVRs require a conventional calibration stage (which will not be detailed here) in order to estimate the bijective polynomial functions f_i that map ϕ_i and V_{LCVRi}, i.e., $\phi_i = f_i(V_{LCVRi})$, with $i = 1, 2$ (An example of such calibration curves is reported in Fig. 10 of the second article of this series [19]). This PSA is positioned in the intermediate image plane between L2 and L3, to minimize the surface of interaction between the light beam and the PSA elements. As described below and in [19], the estimation of the incident Stokes vector $\mathbf{S}^{in} = \left[S_0,\ S_1,\ S_2,\ S_3\right]^T$ is performed from the set of intensity images recorded, each image resulting from the projection of the incident state onto a given analysis polarization state defined by the PSA.

3.3.2. Diaphragm & image sensor

To obtain highly resolved speckle patterns on the camera, a tiny aperture diaphragm (pinhole) of diameter d is placed in front of the detector, on the converging lens nearest to the camera (L3). The average size of a speckle grain is indeed given, in an imaging configuration, as [25]:

$$\delta = 1.22\lambda\frac{2D}{d} \tag{2}$$

where D represents the distance between the detector surface and the upstream lens, which is equal to 6 cm in our configuration. Four sizes of pinholes ranging from 200 to 500 μm in steps of 100 μm were available and were tested in this study.

The detector is a visible silicon graylevel CMOS camera (PHOTONFOCUS A1312) with a full well capacity of 9×10^4 electrons (e$^-$), 4×10^3 e$^-$/s dark current, a readout noise of 110 e$^-$ and a conversion dynamic range of 12 bits, i.e., 4096 grey levels. The sensor has a resolution of 1312 x 1082 pixels, with square pixel size of 8×8 μm. As a result, the typical size of a grain ranges from 0.16 to 0.39 mm on the detector, giving a respective resolution (assuming circular speckle grains) of around 300 pixels per grain to 1900 pixels per grain. Such resolutions ensure in all cases that the speckle pattern is clearly resolved at the speckle grain scale by the sensor, as shown in Fig.1. The choice of the most appropriate diameter $d = 300$ μm and binning factor of 4×4 pixels on the camera are justified below in the next subsection.

3.3.3. Characterization of the speckle grain size

In the experimental context addressed, the choice of the pinhole and speckle size it of utmost importance. There is indeed a compromise between using a small pinhole diameter and ensuring highly resolved speckle fields, but at the expense of a huge limitation of the quantity of light

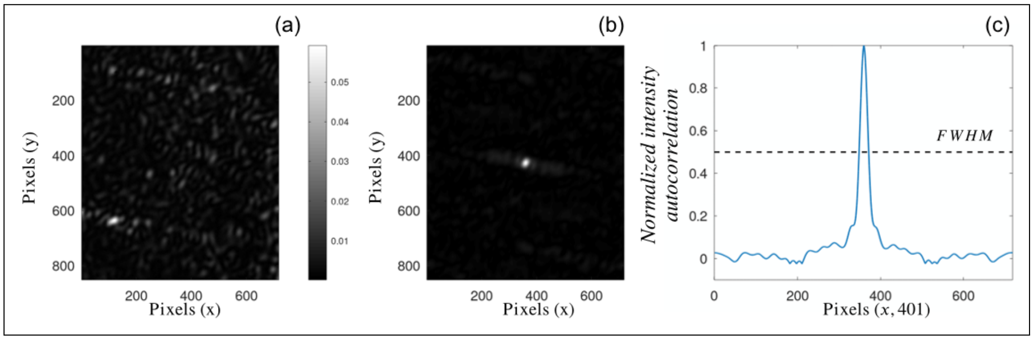

Fig. 4. Experimental estimation of the speckle grain size in pixels at the detector surface with a 300 μm aperture. (a) The intensity image of the speckle pattern averaged over 20 images. (b) Autocorrelation of the speckle pattern. (c) Normalized autocorrelation profile at y=401. The size of the speckle grain is determined by the width at half-height of the autocorrelation peak normalized at y=401.

reaching each pixel, and hence of an increase of exposure time on the camera. We thus experimentally characterized the average speckle grain size without PSA, on a metallic plate, for the 4 different pinholes available. The intensity image of the interference pattern studied, shown in Fig. 4.a for the 300 μm pinhole, results from the averaging of 20 intensity images. The power spectral density (as a function of spatial frequencies ν_x, ν_y) was classically obtained by computing $PSD_I(\nu_x, \nu_y) = |TF\,[I(x, y))]|^2$, with TF denoting 2-D Fourier transform, and $I(x, y)$ denoting the measured intensity at location (x, y) on the camera. Then, the autocorrelation function $R(x, y)$ was finally obtained by inverse Fourier transform of $PSD_I(\nu_x, \nu_y)$ after filtering out the intense zero frequency component (DC). The autocorrelation map obtained is displayed in Fig. 4.b, and the normalized autocorrelation horizontal profile at the center of the image is plotted in Fig. 4.c. The average speckle grain size is then determined by measuring the width at half-height maximum of the normalized autocorrelation function. The average width of a speckle grain is determined for different diaphragm diameters placed successively upstream of the image sensor. These values are shown in Table 1, as well as the corresponding number of pixels per speckle grain (without binning on the camera). All configurations clearly lead to very highly resolved speckle patterns.

However, another experimental parameter that can be adjusted on the camera is the binning factor, which is commonly used to smooth out measurement noise on the detector, but at the expense of a loss in resolution. A thorough study of the influence of the binning factor on the quality of estimation of Stokes vectors has been conducted, but which will not be detailed here for the sake of brevity (see [26] for more details). Such study allowed us to conclude that a 4 × 4 binning factor on the detector was an interesting compromise to diminish estimation variance. As a result, the final choice of parameters that was retained and which will be used throughout this article series correspond to the association of a 4 × 4 binning factor, and a 300 μm pinhole, which leads to approximately 25 binned pixels (also termed *superpixels* below) per speckle grain, thereby ensuring at the same time well resolved speckle patterns, satisfactory noise reduction, and sufficient intensity reaching the detector.

The plot of Fig. 5 allows us to check that this compromise is optimal: on the one hand, above $\sim$ 10 binned pixels (or *superpixels*) per speckle grain, the standard deviation of the Stokes parameters (here S_0) is approximately constant and depends only on the noise characteristics of the camera. On the other hand, for non resolved speckle pattern, the standard deviation does not depend anymore on the number of averaged speckle grains per pixel. In between, the crossover region corresponds to the transition between non resolved speckle patterns and fully resolved ones. As can be seen in Fig. 5, the proposed compromise to use 25 *superpixels* per speckle grain corresponds well to the situation of a resolved speckle field without any influence on estimation precision of the spatial sampling by the camera.

Table 1. **Average speckle grain diameter (in pixels) and average number of pixels per speckle grain as a function of diaphragm diameter.**

Diaphragm diameter (μm)	200	300	400	500
Experimental grain size (pixels)	26	20	18	11
Average number of pixels per grain (no binning)	676	400	324	121

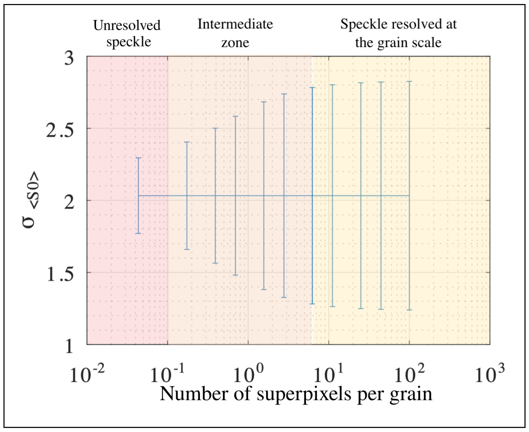

Fig. 5. Representation of the standard deviation of the S_0 parameter as a function of the number of "super" pixels per grain.

3.4. SOPAFP approach and polarization analysis states

In polarimetric imaging, one aims at measuring, at each pixel (i, j) of the image, the Stokes vector $(\mathbf{S}^{in})_{ij}$ ($\mathbf{S}^{in}$ denoting the distribution of the Stokes vector across the whole image). For that purpose, several intensity image measurements are performed on the image sensor, through various configurations of the PSA. At each pixel location (i, j), this process amounts to record a vector of measured intensities $(I_k)_{ij} = \mathbf{S}^T_{PSA,k}.(\mathbf{S}^{in})_{ij}$ which results from the projection of the incident state $(\mathbf{S}^{in})_{ij}$ onto the k^{th} analysis state encoded on the PSA, denoted $\mathbf{S}_{PSA,k}$, where the index k represents the index of the analysis state. Since the process is similar at each pixel location, we will drop out the dependency in (i, j) in the following for clarity reasons. The set of measured intensities can be thus written as a N-dimensional column vector: $\mathbf{I} = [I_1, \cdots, I_k, \cdots, I_N]^T = W\mathbf{S}^{in}$ where W represents the *analysis* matrix, composed of N vectors of the analysis states $\mathbf{S}_{PSA,k}$ ($k \in [1, N]$). Classically, Stokes imaging requires 4 to 6 intensity image measurements and optimal sensing strategies are well-known in these cases [27,28]. Further considerations about Stokes imaging principles, polarization estimation strategies and optimal configurations will be given in Part 2 of this article series [19], and are not presented here for the sake of conciseness.

However, as stated in Section 2, in the context of polarimetric analysis of a highly resolved speckle pattern, the SOPAFP approach was proposed as an alternative sensing method which proved particularly well-suited in this context [18, 24]. Indeed, this technique enables the polarimetric state to be estimated with greater precision while reducing sensitivity to experimental biases. This will be shown in the second paper of this articles series [19], along with a more extensive description of the SOPAFP technique, which basically consists in using numerous (several tens to several hundreds) probe states $\mathbf{S}_{PSA,k}$ distributed over the surface of the Poincaré's sphere. In that case, the set of measures $\{I_1, \cdots, I_k, \cdots, I_N\}$ at a given pixel location can be represented as a particular waveform, which is characteristic of the input Stokes vector $\mathbf{S}^{in}$ to estimate. An example of such waveform is shown in Fig. 6 and consists of the concatenation of 150 intensity measurements obtained on a given set of 150 polarization analysis states generated on the PSA, for a left-handed circular polarization input state.

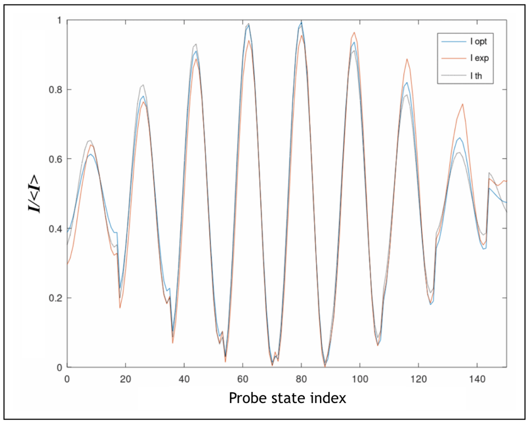

Fig. 6. Averaged intensity curve, normalized by the mean value, over the entire image obtained with a left-hand circularly polarized illumination source and for a given set of 150 projection states. In black: simulated intensity curve theoretically detected by the camera. In red: experimentally measured intensity curve. Blue: optimized intensity curve obtained by non-linear regression.

In [24], it was proposed to estimate the Stokes vector from this characteristic waveform by carrying out a non linear regression of the curve, which can be theoretically expressed as a function of the Stokes vector's parameters (4 parameters) and of the PSA configuration (2 parameters). As detailed in the second article of this series, such non-linear regression is efficient, but very long in terms of computation time, due to the number of pixels in the image sensor (several hundred thousands) and the number of acquisitions (several hundreds). For instance, about 42 minutes were required to process acquisitions of 700×700 pixels undergoing 4×4 binning, for 150 probe states such as the ones implemented in the above example of Fig. 6. As will be shown in the next paper of this series, we have proposed to implement a direct matrix inversion that was shown to have the same estimation performances as the non linear regression , but with a gain in processing time of a factor of 1.5×10^3.

It is well-known in the field of Stokes imaging that estimation errors occuring during inversion of such linear system can be minimized through an appropriate choice of analyzing states which ensure best conditioning of the sensing linear operator (matrix). For instance, in classical Stokes imaging with 4 intensity acquisitions, the optimal states should lie at the vertices of a regular tetrahedron within the Poincaré's sphere. This discussion about the optimal choice of probing states is also reported in the second article of this series, where we demonstrate that even in the context of the SOPAFP approach (i.e., with $N \gg 4$), one can design an optimal set of sensing states to ensure best conditioning of the sensing operator. We will also establish that a set of N=96 measures appears to be a good tradeoff between estimation quality and acquisition/processing delays [19].

4. Automated acquisition protocol

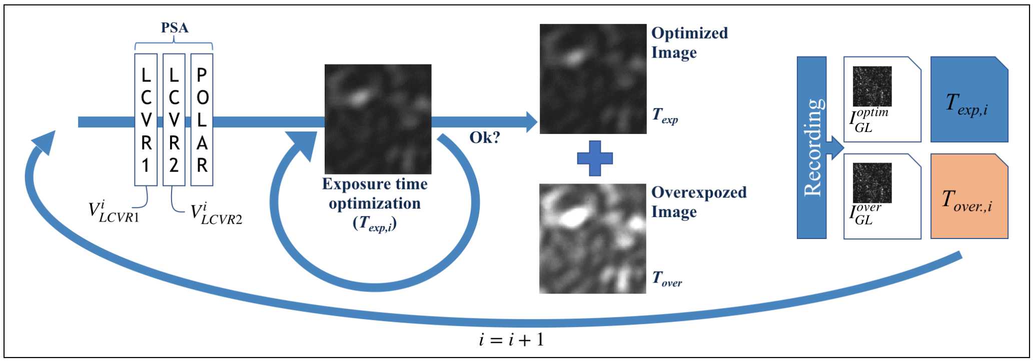

Fig. 7. Schematic diagram of the automated acquisition protocol.

As mentioned above, the acquisition protocol is fully automated and implements a high dynamic range (HDR) imaging approach, in order to increase the dynamic range of the measurement (and thus extend the native 12 bits dynamics of the camera) which is necessary in such a context of imaging an interference pattern composed of very bright and dark spots. This consists in acquiring and appropriately recombining two images, one with optimized exposure time to avoid saturation of the sensor (referred to as optimized image, $I_{\mathrm{GL}}^{\mathrm{optim}}$) and a second image which is overexposed in order to increase the measurement dynamics in the dark regions of the scene (referred to as overexposed image, $I_{\mathrm{GL}}^{\mathrm{over}}$). Control of probe states, HDR acquisition and images recording has been fully automated by computer using the LabVIEW software. The acquisition protocol can be decomposed as follows:

- **Thermalization** : As mentioned previously, before each acquisition, the whole imaging bench is thermalized at 26 °C with laser illumination turned on for about 30 min.
- **Probe states selection**: A voltage pair (V^k_{LCVR1},V^k_{LCVR2}), corresponding to the k^{th} probe state, with $k \in [1, N]$ is applied to the PSA LCVRs plates.
- **Exposure time optimization**: the exposure time is optimized for each image acquisition, through an automated numerical control loop that ensures the following criterion:

  $$90\% \text{ max. sensor dynamics} \leq \max\left\{I_{\mathrm{GL}}\right\} < 100\% \text{ max. sensor dynamics}, \qquad (3)$$

  with I_{GL} denoting the acquired image in graylevel values. This criterion requires that the maximum value of the image (in graylevels) must be less than 100% of the camera dynamic range (in graylevels) to avoid any saturation. In addition, this maximum value must reach at least 90% of the dynamic range, thus guaranteeing the use of a large part of the camera's native dynamic range. The control loop corresponds to a numerical implementation of a PID regulator. The optimized image is then acquired once the exposure time T_{exp} is set.
- **Overexposed image**: A second image is then recorded with a longer exposure time T_{over}, corresponding to the multiplication of the optimized exposure time by an overexposure

coefficient of 4. For these optimization conditions to be fulfilled, it is necessary to ensure the absence of hot pixels on the sensor. These pixels have abnormally high distorted values, generally due to a local defect in the pixel. The camera used in this work has on-board correction processing to overcome these biases by applying a correction based on linear interpolation of the surrounding pixels.

- **HDR recombination**: After acquiring the "optimized" and "overexposed" images and normalizing them by their respective exposure times, they can be recombined, for each pixel of discrete integer coordinates (p, q) as:

$$I^{\text{recomb}}(p,q) = \begin{cases} I^{\text{over}}(p,q) = \frac{I^{\text{over}}(p,q)}{T_{\text{over}}} & \text{if} \quad I^{\text{over}}_{\text{GL}}(p,q) < 4095 \\ I^{\text{optim}}(p,q) = \frac{I^{\text{optim}}(p,q)}{T_{\text{exp}}} & \text{otherwise.} \end{cases} \tag{4}$$

  In this way, the pixel value of the recombined image is equal to that of the normalized overexposed image unless this pixel is saturated, in which latter case the pixel value of the normalized optimized image is selected.

However, this simple recombination procedure was shown to be unsuccessful to provide satisfactory recombined HDR images, which allowed us to identify significant non-linearities in the response of the sensor as a function of illumination and of exposure time. Owing to this imperfection of the sensor, the above HDR recombination was inoperative. Such defects showed that is was necessary to be able to relate the measured graylevels on the camera to calibrated photometric quantities, in order to provide rigorous experimental results and trustful polarimetric state estimations. To overcome this problem, we propose in the next section a camera calibration procedure and intensity image correction protocol that can be applied to any non-linear imaging sensor in order to provide satisfactory photometric measurements.

5. Non-linear sensor calibration/correction procedure

We first detail the calibration protocol that allowed us to estimate the non-linear response of the sensor, and we then report the original image correction technique that was proposed, making it possible to provide reliable photometric measurements from the graylevel pixel data acquired, and to implement a HDR recombination technique.

5.1. Camera calibration

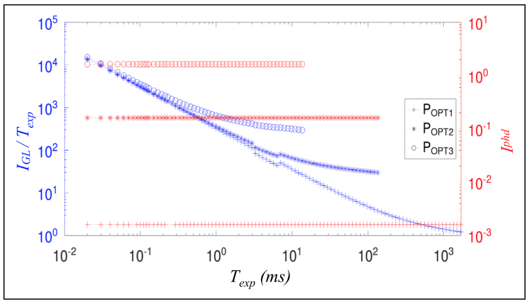

Fig. 8. Measurement of the non-linear intensity response of the camera (average graylevel value normalized by the exposure time, in blue symbols) as a function of the exposure time, for three distinct values of the optical power injected in an integrating sphere. The red symbols correspond to the reference photometric measurement of the light intensity I^{phd} obtained with a calibrated photodiode.

The characterization of the non-linear response of the camera was carried out using the illumination laser which was injected in one port of a 40 cm diameter integrating sphere (LABSPHERE). The CMOS focal plane was placed in front of the main port (5 cm diameter) of the integrating sphere, thereby enabling perfectly homogeneous and isotropic illumination of the sensor due to strong scattering of the incident beam by the integrating sphere coated with highly scattering Spectralon. The sphere was equipped with a reference photodiode located inside the sphere, and coupled to a pico-amperemeter (KEITHLEY) providing us with a trustful and calibrated (albeit relative) measurement of the photometric intensity on the sensor. In Fig. 8, one can observe the strong non-linearity of the sensor since, at a given power, the ratio of intensity normalized by the exposure time T_{exp} is not constant. For a camera with a linear response, the normalized graylevel intensity should be constant at a constant power, which is not the case for our sensor, hence highlighting the non-linear nature of the intensity (greyscale) response as a function of exposure time of our camera. To fully characterize the camera non-linearities, an automated protocol was implemented to simultaneously measure the camera intensity in graylevels I_{GL} (average over the whole sensor) and the photometric intensity I_{phd} measured with the photodiode, while performing a slow sweep of the laser power P_{opt} coupled with a fast sweep of the camera exposure time T_{exp} (ranging from durations of 0.01 to 1667 ms). In this way, 8×10^3 calibration points were measured and recorded. The 12-bit greylevel values measured on the camera are displayed in Fig. 9 for these 8×10^3 calibration points, as a function of the exposure time, and for various illumination powers. A corresponding 2-D map was obtained for the 8×10^3 calibration points, providing the photometric intensity value measured on the reference photodiode as a function of illumination power. These two mappings allow us to design an automated and fast correction protocol for all the image acquisitions performed after this calibration step.

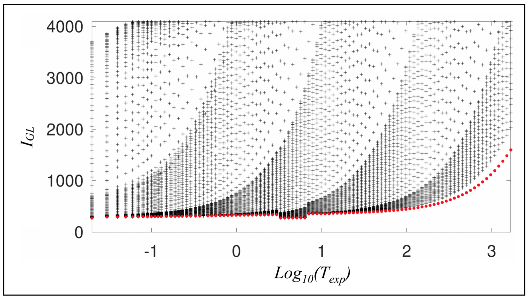

Fig. 9. Plot of the graylevel values (12 bits) measured by the camera as a function of exposure time for various illumination powers.

5.2. Correction protocol

The above calibration experiment provided us with two mappings of the camera intensity in graylevel and of the photometric intensity measured by calibration. The 8×10^3 calibration points are located in a non-regular grid mapping the experimental parameters: exposure time and optical power. In order to be able to correct acquired data at each pixel for any situation, it is necessary to interpolate such calibration set. This was operated by first computing a Delaunay tesselation mesh on this calibration data, followed by a linear data interpolation step. The whole calibration/correction processing comprises four main steps:

- **Computation of the Delaunay's triangulation mesh**: The calibration procedure proposed relies on the computation of a Delaunay triangulation mesh between calibration datapoints in the ($\log(T_{\mathrm{exp}})$, I_{GL}) plane (see Fig. 9). Such operation is also referred to as Delaunay tesselation, which consists of connecting all the data points with a triangular mesh that is optimized so to as to avoid sliver triangles [29].

As the 8×10^3 calibration points are spread over 5 decades of T_{exp}, and in order to minimize the processing time, it appeared irrelevant to use the whole calibration data set (which would hav implied computing and handling a huge amount of data in the recorded mesh) to process each pixel value of each acquired image. We thus rather computed “local” meshes from subsets of the calibration data in the vicinity of the actual frame exposure time T_{exp} as shown in Fig. 10 b. This subset is defined as follows:

$$\left\{ i \in \left[1; 8\times10^3\right] \quad / \quad \log(T_{\text{exp}}) - 0.1 \leq \log(T^{\text{cal}}_{\text{exp,i}}) \leq \log(T_{\text{exp}}) + 0.1 \right\} \tag{5}$$

with log denoting decimal logarithm, and where T_{exp} is the exposure time of the image/pixel to be processed, and $T^{\text{cal}}_{\text{exp,i}}$ is the exposure time of the i^{th} calibration point. A Delaunay tessellation mesh is then calculated on the selected calibration points (Fig. 10.b), and stored in the computer for further image correction. It can be noted that this calibration step has to be performed only once, since the recorded meshs can be then used later on for images correction steps detailed below.

- **Positioning pixel value in the calibration mesh**: For the pixel with coordinates (p,q) in the sensor, the greyscale intensity value to be corrected $I_{\text{GL}}(\text{p},\text{q})$ is positioned in the $(\log(T_{\text{exp}}), I_{GL})$ plane (see Fig. 10.a).
- **Mesh cell identification** : The coordinates of the three vertices of the mesh surrounding $I_{\text{GL}}(\text{p},\text{q})$ in the $(\log(T_{\text{exp}}), I_{\text{GL}})$ plane are determined (see Fig. 10.b).
- **Data interpolation and photometric correction**: Finally, the corrected photometric intensity value $I_{\text{corr}}(\text{p},\text{q})$ is obtained using a linear interpolation in triangular coordinates of the calibration data available at the three vertices (see Fig. 10.c).

To perform HDR imaging, this correction protocol has to be applied a second time for the pixels corresponding to the overexposed image, hence requiring the use of a second "local" Delaunay mesh stored from calibration. HDR recombination must now be carried out on the corrected images, using the same criterion as in Eq. (6):

$$I^{\text{recomb}}_{\text{corr}}(p,q) = \begin{cases} I^{\text{over}}_{\text{corr}}(p,q) & \text{if} \quad I^{\text{over}}_{\text{GL}}(p,q) < 4095 \\ I^{\text{optim}}_{\text{corr}}(p,q) & \text{otherwise.} \end{cases} \tag{6}$$

The advantage of this calibration/correction method is that it makes it possible to convert (non-linear) camera greyscale data into a photometric quantity (relative, but guaranteeing good linearity), while preserving the advantages of the HDR approach. This generic approach could be applied to any type of camera, to the expense of a meticulous and time-consuming calibration stage, but with calibration datapoints that are not necessarily on a regular grid. The proposed correction procedure sufficiently fast in the context of this study where real-time imaging and processing is not required (typically 1.3 seconds required for correcting a 700 × 700 pixel image).

5.3. Validation of the calibration/correction protocol

In order to assess the effectiveness of the calibration/correction protocol proposed above for correcting the non-linearity of the sensor, a first validation was carried out on a subset of calibration data points. First, we removed from the calibration dataset (Fig. 9) all calibration points corresponding to a constant relative photometric intensity of $I_{phd} = 1.633$. The selected points were considered as a test dataset, while the remainder of the calibration points were used as

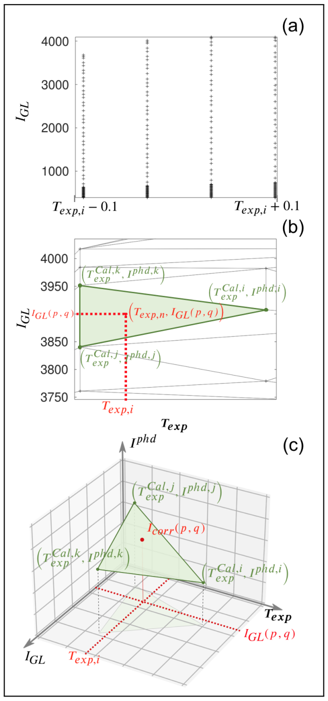

Fig. 10. Illustration of the correction protocol proposed to convert the grayscale value $I_{\mathrm{GL}}(p,q)$, detected at pixel (p,q) for an exposure time T_{exp}, into a calibrated photometric intensity value $I_{\mathrm{corr}}(p,q)$. For the sake of readability, a logarithmic scale is used for the exposure times

the calibration dataset for this validation step. Secondly, the entire correction protocol (Delaunay tesselation and linear interpolation in triangular coordinates) was applied to correct the test dataset from the calibration dataset, and to compute photometric corrected intensity values I_{corr}. This allowed us to compare these corrected intensity values to the ground-truth photometric intensity measurements available in the original calibration dataset. Such comparison is shown in Fig. 11, where it can be seen that, for a constant photometric intensity value of $I_{phd} = 1.633$ (black diamonds and dotted line), the range of corrected intensity values lies within a 5.4‰ margin from the calibrated photometric value (black triangles). This plot demonstrates the efficiency of the calibration/correction protocol proposed to ensure reliable photometric quantities in the measured images, while simple normalization of the greylevel values by the exposure time is very inoperative with such a non-linear sensor (red circles).

A further validation step on experimental data was conducted to prove the relevance of this protocol, as well as the efficiency of the HDR recombination. The calibration/correction protocol was applied to Stokes imaging data, obtained experimentally on a metallic plate probed by 80 polarimetric states distributed uniformly over the Poincaré's sphere, with a binning factor of 4×4 pixels, and with the dual exposure time HDR approach detailed above. From this polarimetric data, we computed the S_0 image (total intensity) plotted in Fig. 12 ((a) and (e)), the map of the DOP ((b) and (f)), and its corresponding histogram ((c) and (g)). The first row of Fig. 12 corresponds to the results obtained when the acquired images are simply normalized by their respective exposure time and with HDR recombination using Eq. (4), whereas the second row corresponds to data after correction of the sensor's non-linearities and HDR recombination through Eq. (6). Although no clear difference can be observed between the intensity images ((a) and (e)), the

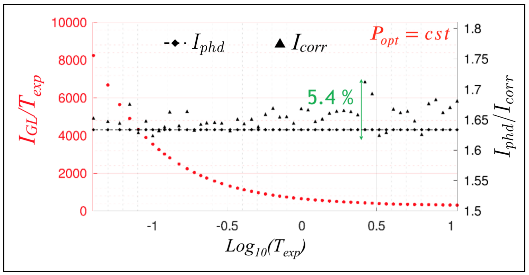

Fig. 11. Graphical comparison between the greyscale intensity values of the selected points normalized by the respective exposure time I_{GL}/T_{exp} (red circles), the intensity value after correction I_{corr} (black triangles) and the relative photometric intensity I_{phd} (black diamonds and dotted horizontal line).

maps of the DOP clearly demonstrates the necessity of the non-linear calibration/correction stage. Indeed, as expected on a non-depolarizing sample (such as a metallic blade) illuminated with linearly polarized light, the DOP value should be equal to one over the whole field of view (at least in significantly bright regions where the estimation of the state of polarization can be trusted). This is clearly not the case when the data is not preliminary corrected before HDR recombination, the histogram of the DOP showing a clearly unexpected bimodal behaviour with an average value of 0.27. Much more satisfactory are the map and histogram of the DOP obtained (on the same experimental data acquisition) after photometric correction: a majority of pixels show high value of the DOP, as expected, with an average value of 0.74 and with very few abnormal data (only about 1.2% of the pixels having an unphysical estimated DOP value above 1). In order to confirm the efficiency of the correction approach implemented, and to demonstrate the fact that low values of DOP are obtained in low intensity regions where the estimation of the Stokes parameters is less reliable, scatter plots displaying the estimated value of the DOP at each location of the image as a function of the S_0 value are provided in Fig. 12 (d) and (h). First, the analysis of the plot of Fig. 12 (d) confirms the inability of the simple normalization by exposure time to provide satisfactory maps of the DOP. Then, it can be seen in Fig. 12 (h) that the correction approach leads to a much more trustworthy distribution of the DOP (expected to be unitary across the image for a metallic non depolarizing plate under polarized illumination), where low values of the DOP are clearly obtained for low values of the S_0 intensity across the speckle pattern. Finally, as these results are in agreement with anterior studies [16], we consider that these results validate the efficiency of the proposed calibration/correction protocol.

In the next section, and in all the remainder of this article series, this calibration/correction processing scheme will be applied to all experimental data reported. Of course, the calibration/correction protocol described above would be unnecessary when using a camera with a satisfactory linear response of its graylevels with illumination power and exposure time, thereby saving some post-processing time. However, such a calibration/correction technique can prove interesting in any imaging context where relevant relative photometric measures are required, and in particular in spectral domains where the sensors technology is less mature than in the visible range.

6. Preliminary results and validation of the experimental setup

In the last section of this paper, we briefly illustrate the relevance of the choices discussed above for the various experimental parameters at stakes for Stokes polarimetric analysis resolved at the speckle grain scale. Stokes imaging results obtained on two samples are presented below: on a metallic plate (non-depolarizing sample) and on a sample of Spectralon (totally depolarizing

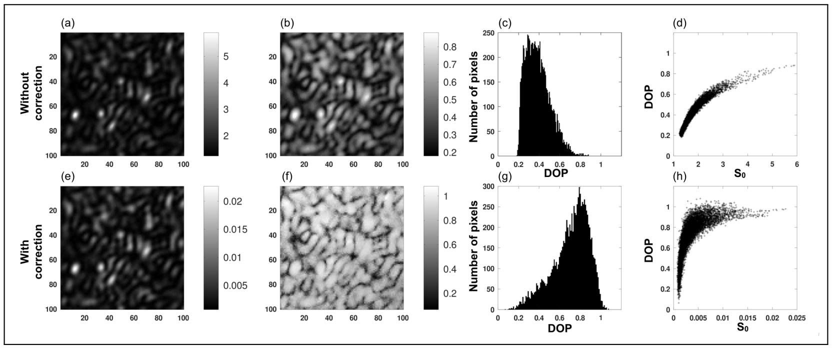

Fig. 12. Experimental images of S_0 (first column), DOP (second column) and histogram of the DOP (third column) without correction (respectively (a), (b), (c)), and after application of the correction protocol (respectively (e), (f), (g)). The scatter plots displayed in (d) and (h) show the correlation of the measured DOP values with the speckle field intensity S_0 respectively before and after correction.

scattering sample). These acquisitions were made with a vertically polarized input light beam and a diaphragm diameter of 300 μm. For Stokes measurements, $N = 80$ polarimetric states uniformly distributed over the surface of the Poincaré's sphere, according to the above mentioned SOPAFP approach, are probed using the liquid crystal variable delay plate PSA. In addition, the two-image HDR approach described in Section 4 is used during acquisition, and the grey-scale intensity images are recombined and corrected to obtain photometric intensity images, as stated above in the description of the calibration process. A 4×4 pixel binning factor is used before estimation of the various Stokes parameters and of the DOP, which are deduced from these intensity images.

These first validation results are presented in Fig. 13 for both samples (metallic plate on the left-hand side, spectralon on the right-hand side). Plots of Fig. 13 display examples of intensity acquisitions (S_0) in graylevels in the first row. Then, the two next components s_1 and s_2 of the reduced Stokes vector (i.e., Stokes vector normalized by the value of S_0) are mapped in the second and third rows, with values between -1 and 1 represented with a green/pink colormap. The last component s_3 of the reduced Stokes vector, corresponding to the circular polarization contribution, is mapped in the fourth row, with values between -1 and 1 represented with a specific blue/red colormap, red color (respectively blue) denoting right (respectively left) circular polarization, i.e. negative (respectively positive) ellipticity. Finally, the DOP is computed and plotted in the last row in graylevels. These plots are analyzed below:

6.1. Metal plate

The first sample considered is a flat, metallic plate roughly polished so that it can scatter light at its surface, even at a non-specular angle, thereby producing a speckle field that can be imaged in the setup. Although such metallic rough surface can locally introduce retardance due to its complex refractive index at oblique incidences, we will consider in first approximation that this sample almost does not alter the polarization state of the incident light, which is linearly vertically polarized. As a result, only the s_1 component should differ from zero, with unit value. This is what is observed in the left column of Fig. 13, with very small values of s_2 and s_3, while s_1 is almost uniformly very close to 1, at least in significantly bright regions of the speckle pattern. In very dark regions indeed, despite the HDR approach implemented, the level of confidence in the estimated values of the Stokes components is lower. Another interesting feature of non-depolarizing samples is that the speckle pattern spatial distribution should be

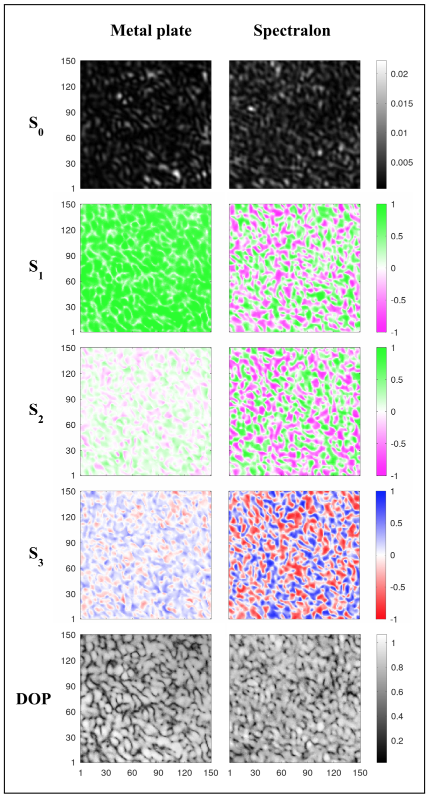

Fig. 13. Images of the various Stokes parameters and DOP determined for a sample corresponding to a metal plate in the left column and Spectralon in the right.

independent of the probe states, and hence should be the same in the various maps of the Stokes parameters [16, 30]. Although this is rather difficult to observe in the plots of Fig. 13, we have analyzed the comparative spatial distribution of the speckle pattern intensity for various analyzing states, and of the Stokes parameters maps, and we have experimentally checked that the speckle spatial distribution was not significantly modified during the whole set of acquisitions, thereby demonstrating the validity of our setup to preserve the analyzed complex wavefront throughout the measurement.

Lastly, it can also be checked that the local DOP in the last row shows values very close to 1 in the constructive interference zones (sufficiently bright regions), which is in agreement with initial observations in [16].

6.2. Spectralon

The depolarizing nature of the Spectralon sample is due to its high reflectivity (reflectance of 99%) and its complex microstructure which allows multiple bulk scattering of light within a thin layer of the material. Such multiple scattering events induce a local modification of the incident polarization state uniformly across the Poincaré's sphere, leading to a strong and total spatial depolarization when the local polarization states are coherently averaged over the surface of a single detector for instance. This is clearly observed in the maps of the s_1, s_2 and s_3 parameters provided in Fig. 13, confirming the depolarizing nature of this sample. As before, the DOP image shows values close to 1 in the constructive interference zones, corresponding to the fact that the polarization state within a grain is deterministic, in agreement with anterior observations [16, 23].

In view of the displayed patterns of the different Stokes parameters, we observe a rapid spatial variation of the polarization state across the speckle pattern. This will be of particular interest in the last paper of this article series for the study of the polarization behaviour across a speckle field and in the vicinity of polarimetric singularities.

7. Conclusion

In this article, the implementation of an optimized polarimetric Stokes imaging bench resolved at the speckle grain scale was described, along with a justification of all the choices of experimental parameters used. The set of parameters described above will be considered in the remainder of this article series, either for the theoretical/numerical study of the second paper, or for the experimental results and analyses presented in the third paper. In the next paper of this series, we conduct a theoretical study and numerical simulation analysis in order to demonstrate the validity of the SOPAFP approach to provide optimal precision and accuracy of Stokes measurements, and its superiority with respect to standard approaches in terms of robustness of the estimation results in the presence of experimental defects in the setup.

Acknowledgments. The authors would like to thank the DOP team and in particular Mehdi Alouini, Goulc'hen Loas for fruitful discussions and Steve Bouhier for technical help.

Disclosures. The authors declare no conflicts of interest.

Data availability. Data underlying the results presented in this paper are not publicly available at this time but may be obtained from the authors upon reasonable request.

References

1. J. S. Lim and H. Nawab, "Techniques for speckle noise removal," in *Applications of speckle phenomena,* vol. 243 (SPIE, 1980), pp. 35–45.
2. B. Daino, G. De Marchis, and S. Piazzolla, "Speckle and modal noise in optical fibres theory and experiment," Opt. Acta: Int. J. Opt. **27**, 1151–1159 (1980).
3. J. M. Schmitt, S. Xiang, and K. M. Yung, "Speckle in optical coherence tomography," J. biomedical optics **4**, 95–105 (1999).
4. S. Xiang, L. Zhou, and J. M. Schmitt, "Speckle noise reduction for optical coherence tomography," in *Optical and Imaging Techniques for Biomonitoring III,* vol. 3196 (SPIE, 1998), pp. 79–88.
5. D. A. Boas and A. K. Dunn, "Laser speckle contrast imaging in biomedical optics," J. biomedical optics **15**, 011109–011109 (2010).
6. P. G. Vaz, A. Humeau-Heurtier, E. Figueiras, C. Correia, and J. Cardoso, "Laser speckle imaging to monitor microvascular blood flow: a review," IEEE reviews biomedical engineering **9**, 106–120 (2016).
7. J. Shamir, "Speckle polarization investigated by novel ellipsometry," Opt. Eng. **25**, 618–622 (1986).
8. İ. İ. Tarhan and G. H. Watson, "Polarization microstatistics of laser speckle," Phys. Rev. A **45**, 6013 (1992).
9. P. Elies, B. Le Jeune, F. Le Roy-Brehonnet, J. Cariou, and J. Lotrian, "Experimental investigation of the speckle polarization for a polished aluminium sample," J. Phys. D: Appl. Phys. **30**, 29 (1997).
10. D. Briers, D. D. Duncan, E. Hirst, S. J. Kirkpatrick, M. Larsson, W. Steenbergen, T. Stromberg, and O. B. Thompson, "Laser speckle contrast imaging: theoretical and practical limitations," J. biomedical optics **18**, 066018–066018 (2013).
11. W. Heeman, W. Steenbergen, G. M. van Dam, and E. C. Boerma, "Clinical applications of laser speckle contrast imaging: a review," J. biomedical optics **24**, 080901–080901 (2019).
12. L. Tchvialeva, G. Dhadwal, H. Lui, S. Kalia, H. Zeng, D. I. McLean, and T. K. Lee, "Polarization speckle imaging as a potential technique for in vivo skin cancer detection," J. biomedical optics **18**, 061211–061211 (2013).
13. M. Zerrad, H. Tortel, G. Soriano, A. Ghabbach, and C. Amra, "Spatial depolarization of light from the bulks: electromagnetic prediction," Opt. Express **23**, 8246–8260 (2015).
14. K. Hinsch, T. Fricke-Begemann, G. Gülker, and K. Wolff, "Speckle correlation for the analysis of random processes at rough surfaces," Opt. Lasers Eng. **33**, 87–105 (2000).
15. P. Hariharan, "Statistics of speckle patterns produced by a rough metal surface," Opt. Acta: Int. J. Opt. **24**, 979–987 (1977).
16. L. Pouget, J. Fade, C. Hamel, and M. Alouini, "Polarimetric imaging beyond the speckle grain scale," Appl. optics **51**, 7345–7356 (2012).

17. A. Ghabbach, M. Zerrad, G. Soriano, and C. Amra, “Accurate metrology of polarization curves measured at the speckle size of visible light scattering,” Opt. Express **22**, 14594–14609 (2014).
18. J. Dupont, X. Orlik, A. Ghabbach, M. Zerrad, G. Soriano, and C. Amra, “Polarization analysis of speckle field below its transverse correlation width: application to surface and bulk scattering,” Opt. Express **22**, 24133–24141 (2014).
19. J. Staes and J. Fade, “Optimized stokes imaging for highly resolved optical speckle fields, part II: Optimal acquisition & estimation strategies,” submitted to J. Opt. Soc. Am. A (2024).
20. J. Staes and J. Fade, “Optimized stokes imaging for highly resolved optical speckle fields, part III: Optimized polarimetric data representation & topological polarimetric analysis,” submitted to J. Opt. Soc. Am. A (2024).
21. D. H. Goldstein, *Polarized light* (CRC press, 2017).
22. J. Sorrentini, M. Zerrad, G. Soriano, and C. Amra, “Enpolarization of light by scattering media,” Opt. Express **19**, 21313–21320 (2011).
23. A. Ghabbach, M. Zerrad, G. Soriano, S. Liukaityte, and C. Amra, “Depolarization and enpolarization dop histograms measured for surface and bulk speckle patterns,” Opt. express **22**, 21427–21440 (2014).
24. J. Dupont and X. Orlik, “Speckle fields polarimetry: statistical analysis and polarization singularities measurements,” in *SPECKLE 2015: VI International Conference on Speckle Metrology,* vol. 9660 (SPIE, 2015), pp. 259–269.
25. J. W. Goodman and P. Sutton, “Introduction to fourier optics,” Quantum Semiclassical Opt. Eur. Opt. Soc. Part B **8**, 1095 (1996).
26. J. Staes, “Imagerie polarimétrique et physique de dépolarisation lumineuse: polarimétrie de champs de speckle ultra-résolus et approches optique-hyperfréquences,” Ph.D. thesis, Université Rennes 1 (2022).
27. J. S. Tyo, “Design of optimal polarimeters: maximization of signal-to-noise ratio and minimization of systematic error,” Appl. optics **41**, 619–630 (2002).
28. A. Peinado, A. Lizana, J. Vidal, C. Iemmi, and J. Campos, “Optimization and performance criteria of a stokes polarimeter based on two variable retarders,” Opt. express **18**, 9815–9830 (2010).
29. B. Delaunay *et al.*, “Sur la sphere vide,” Izv. Akad. Nauk SSSR, Otdelenie Matematicheskii i Estestvennyka Nauk **7**, 1–2 (1934).
30. M. Roche, J. Fade, and P. Réfrégier, “Parametric estimation of the square degree of polarization from two intensity images degraded by fully developed speckle noise,” J. Opt. Soc. Am. A **24**, 2719–2727 (2007).